

Systematic study of rotational decoherence with a trapped-ion planar rotor

Neil Glikin,^{1,2} Benjamin A. Stickler,³ Ryan Tollesen,^{1,2} Sara Mouradian,⁴
Neha Yadav,^{1,2} Erik Urban,^{1,*} Klaus Hornberger,⁵ and Hartmut Haeffner^{1,2}

¹*Department of Physics, University of California, Berkeley, Berkeley, California 94720, USA*

²*Challenge Institute for Quantum Computation, University of California, Berkeley, Berkeley, California 94720, USA*

³*Institute for Complex Quantum Systems, Ulm University, Albert-Einstein-Allee 11, 89069 Ulm, Germany*

⁴*Department of Electrical and Computer Engineering,*

University of Washington, Seattle, Washington 98195, USA

⁵*University of Duisburg-Essen, Faculty of Physics, Lotharstraße 1, 47057 Duisburg, Germany*

Quantum rotors promise unique advantages for quantum sensing, quantum simulation, and quantum information processing. At present, a variety of systems ranging from nanoparticles to single molecules and trapped ions have demonstrated detection and control of rotational motion in and near the quantum regime. For future applications of quantum rotors, understanding their dynamics in the presence of ambient environments and decoherence will be critical. While other model quantum systems such as the harmonic oscillator have seen extensive experimental study of their decoherence dynamics, such experiments remain an open task for the rigid rotor. We present measurements of fundamental scaling relationships for decoherence of a quantum planar rotor realized with two trapped ions, and find excellent agreement with recent theoretical work.

The quantum rigid rotor is among the simplest model quantum systems, on par with the quantum harmonic oscillator and the qubit. In contrast to these, the technological potential of quantum rotor dynamics has not yet been fully tapped. There have recently been remarkable advances in the preparation and control of molecular rotational states [1–7], in using such states for coherent interactions [8–12], and in the manipulation of nanoscale rotors [13–18]. These developments are motivated by prospects of using the unique properties of rotors for encoding quantum information [19–21], performing quantum simulations using tunable dipole-dipole interactions [22–24], torque sensing [14], and tests of the quantum superposition principle at high masses [25, 26].

Experiments which aim to exploit rotational quantum coherence will also need to contend with interaction with their environment and the resulting decoherence. In rotor systems, decoherence has been experimentally observed only in certain limited contexts. These include the decay of rotational coherences in gas-phase ensembles of molecules due to collisions or radiation [27–31], and due to light scattering or uncontrolled differential shifts in optical traps [8, 12, 32–35]. To push quantum rotors into a useful coherent regime, a comprehensive understanding of their decoherence dynamics will be crucial.

The theory of rotor decoherence, which fully accounts for orientational periodicity, has been developed only within the last decade [36–40]. An important case is interaction with an isotropic environment, which leads to diffusion of a rotor’s angular momentum state. In this case, a superposition of two orientation states $|\phi\rangle + |\phi'\rangle$ is predicted to decay into a statistical mixture at a rate proportional to two important parameters: (i) the angular

momentum diffusion coefficient, and (ii) for inversion-symmetric planar rotors, the sine squared of their relative angle, $\sin^2(\phi - \phi')$. This can be compared with the decoherence rate $|\alpha - \alpha'|^2$ for a superposition of harmonic oscillator coherent states $|\alpha\rangle + |\alpha'\rangle$ [41]. Experimentally verifying harmonic oscillator decoherence scalings [42–44] proved crucial for developing oscillators into building blocks for quantum technologies. For rotors, the analogous relations have not yet been experimentally probed.

Here we report on a systematic study of the decoherence dynamics of a planar rigid rotor. The rotor is composed of two trapped atomic ions separated by several micrometers and rotating with a frequency on the order of one hundred kilohertz. We prepare this system in a superposition of different rotation rates, which turns into a superposition of orientation states, and engineer a noisy electric-field environment to induce rotational decoherence on the millisecond timescale. Our results demonstrate a sine-squared scaling of the decoherence rate for orientational superpositions in the small-angle limit and the expected scaling with the angular momentum diffusion coefficient. Both findings are in excellent agreement with theory.

This work will be relevant for future studies of the prospects and practical challenges of fault-tolerant quantum information processing with rotors [20, 21], of decoherence-free subspaces of orientation states [45], and of macroscopic quantum tests with nanorotors [25, 26]. Moreover, it constitutes a first step towards systematically probing surface-induced heating and decoherence of rotors that are characterized by charge multipoles [46].

We realize a quantum rigid rotor as a pair of $^{40}\text{Ca}^+$ ions Paul-trapped in a cylindrically symmetric potential, created by a surface ion trap with circular radio-frequency (rf) electrodes. The electrodes produce a three-dimensional harmonic potential centered 180 μm above the trap surface, whose confinement strength is characterized by secular trap frequencies $\omega_z = 2\pi \times 2.87 \text{ MHz}$

* Current address: Exponent, Inc., Electrical Engineering and Computer Science Practice, Warrenville, IL

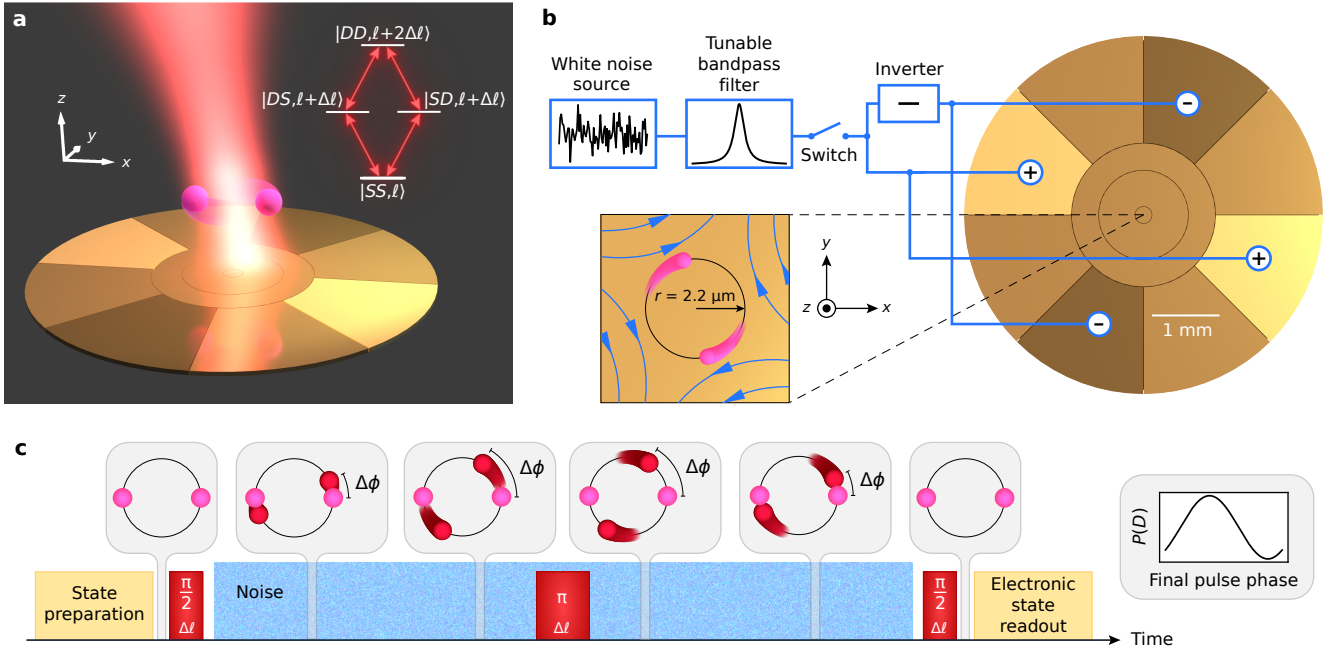


Fig. 1. Experimental setup and sequence. **a**, Two $^{40}\text{Ca}^+$ ions (not to scale) rotate above a circular surface ion trap in the plane parallel to the surface. A tilted vertical beam of 729 nm laser light addresses the ion crystal on rotational sidebands of the electronic $|S\rangle \leftrightarrow |D\rangle$ transition, labeled by their order $\Delta\ell$, to create angular momentum superpositions. Sidebands of different orders $\Delta\ell$ are spectrally resolved from one another. $|SS, \ell\rangle$ denotes a state with both ions in the electronic $|S\rangle$ state and with rotor angular momentum $\hbar\ell$. **b**, Circuit schematic of the setup for creating the electric-field gradient noise environment. A narrowband noisy voltage is applied to the outer control electrodes in an alternating pattern, giving rise to a quadrupole electric field at the location of the ion rotor. The zoom-in shows the ion rotor and the quadrupole field (blue). The noisy gradient of this field exerts random torques on the rotor when on resonance with the ions' rotation, resulting in angular momentum diffusion and decoherence. **c**, Simplified diagram of the Ramsey sequence used to measure rotational decoherence. Ions are shown in a co-rotating frame. A $\pi/2$ pulse from the 729 nm laser on a rotational sideband of order $\Delta\ell$ creates a superposition of angular momenta. This may be equated to a superposition of two orientations of the rotor which are freely evolving at different angular velocities and have a linearly increasing angular separation $\Delta\phi$. A π pulse reverses the separation, and a $\pi/2$ pulse closes the interferometer. The electric field gradient noise environment is turned on while the interferometer is open. The remaining orientational coherence is mapped to the electronic state, and is quantified as the amplitude of the interference fringe.

normal to the trap surface and $\omega_x = \omega_y = 2\pi \times 1.44 \text{ MHz}$ in the transverse plane. Since $\omega_z > \omega_{x,y}$, the ions are confined to the transverse plane, while the cylindrical symmetry allows for a free rotational motion of the ion crystal within the plane [47, 48]. The ions' mutual Coulomb repulsion balanced with the trap potential creates a rigid rotor with a calculated radius $r = 2.2 \mu\text{m}$. Non-rigid corrections are of order 10^{-2} and are negligible (see Methods).

The Hamiltonian describing the rotational motion of the ion crystal is that of a planar rotor $H_0 = L_z^2/2I$, where L_z is the angular momentum operator component normal to the rotor plane and $I = 2mr^2$ is the moment of inertia. The angular momentum eigenstates $|\ell\rangle$ are simultaneous eigenstates of the Hamiltonian H_0 and the angular momentum operator L_z , with angular momentum eigenvalues $\hbar\ell$ where ℓ takes integer values. The energy scale is set by the rotational constant $\omega_r = \hbar/2I = 2\pi \times 13 \text{ Hz}$, equal to the transition frequency between the ground and first excited rotational states.

Each ion contains an independent electronic degree of freedom, of which only two states are of interest: the $^2S_{1/2}$ ($m = -1/2$) sublevel of the ground electronic state (labelled $|S\rangle$) and the metastable $^2D_{5/2}$ ($m = -1/2$) state (labelled $|D\rangle$). The ions' internal electronic states are coherently manipulated by a narrow-linewidth laser near the $|S\rangle \leftrightarrow |D\rangle$ resonance at 729 nm. Sidebands of this resonance are used to couple to the rotational degree of freedom. The 729 nm laser addresses the full ion crystal nearly normal to the rotor, at a small angle of 5.6° with respect to the normal of the rotor plane, in order to maximize coupling to the desired sideband orders [48]. A uniform magnetic field of 409 pT separates the Zeeman sublevels of the electronic states to allow frequency selectivity of the sublevels of interest. State measurement is performed by applying cycling transition laser light at 397 nm, which is resonant with a dipole-allowed transition from the $|S\rangle$ state but off-resonant from any transition from the $|D\rangle$ state. This allows state discrimination by counting scattered photons. All measurements record

the $|D\rangle$ state population averaged between the two ions, $P(D)$.

We experimentally realize a controllable environment by applying a noisy voltage to the outer control electrodes of the trap, giving rise to a noisy electric field that couples to the rotor via the ions' charge. Since the two-ion crystal has zero dipole moment, the interaction with the noise field is via its quadrupole component and thus is proportional to the local field gradients. We inject voltage noise onto four of the eight control electrodes which surround the rf electrodes with alternating sign, as shown in Fig. 1b. The resulting quadrupole field is proportional to the applied voltage, which is generated as white noise from an arbitrary waveform generator and passed through a bandpass filter with a 19 kHz bandwidth and tunable center frequency. This allows us to directly control the noise spectral density of the electric field gradient. In the absence of injected voltage noise, uncontrolled ambient electric field gradient noise is still present at the location of the ions due to stray voltage noise and thermally induced field fluctuations originating from the electrodes [46, 49].

Averaging the rotor-field interaction over many realizations of the noisy electric field gradient, the dynamics of the rotor's quantum state ρ are described by the Lindblad master equation of orientational decoherence for quadrupolar interactions $\partial_t \rho = -i[H_0, \rho]/\hbar + \mathcal{L}\rho$ with (see Methods),

$$\mathcal{L}\rho = \frac{D}{4\hbar^2} (L_-^2 \rho L_+^2 + L_+^2 \rho L_-^2 - 2\rho). \quad (1)$$

Here, L_{\pm} are dimensionless angular momentum raising and lowering operators, $L_{\pm}|\ell\rangle = |\ell \pm 1\rangle$. The master equation describes angular momentum diffusion at a rate D , i.e. $\partial_t \langle L_z^2 \rangle = 2D$, and decoherence in the rotor orientation ϕ [38],

$$\langle \phi | \mathcal{L}\rho | \phi' \rangle = -\frac{D}{\hbar^2} \sin^2(\phi - \phi') \langle \phi | \rho | \phi' \rangle. \quad (2)$$

The scaling with $\sin^2(\phi - \phi')$ is π -periodic rather than 2π -periodic due to the inversion symmetry of the quadrupole interaction [38, 45]. For a rapidly spinning rotor with mean angular frequency $\omega_{\text{rot}} = \langle L_z \rangle / I$, the diffusion coefficient is determined by the power spectral density of the field gradient at twice the rotation frequency,

$$D = \left(\frac{er^2}{2} \right)^2 S_{\varepsilon}(2\omega_{\text{rot}}). \quad (3)$$

Here, $S_{\varepsilon}(\omega)$ is the power spectral density of $\varepsilon_t = -\partial_x E_x + \partial_y E_y + 2i\partial_x E_y$, which is the relevant field gradient for quadrupolar interaction in the plane parallel to the surface (see Methods). The environment does not induce rotational friction within measurement limits (see Methods), and thus friction terms [39] are omitted from the master equation (1).

We present two types of measurements, (i) angular momentum diffusion of the quantum rotor, and (ii) decoherence of angular momentum superpositions. In both

cases, we begin with the ions trapped in an additional pinning potential which fixes their locations. We first cool all motional degrees of freedom with Doppler cooling, then sideband cool the transverse librational motion and the motion normal to the rotor plane. We then initialize the ions' internal states to $|S\rangle$ via optical pumping, and spin up the rotor by rotating and then releasing the pinning potential via a protocol described in Ref. [48]. This approximately produces a coherent rotor state $|\Psi_{\bar{\ell}}\rangle$ that is localized in angular momentum space at $\bar{\ell} = \langle L_z \rangle / \hbar \gg \sigma_{\ell}$, where σ_{ℓ} is the standard deviation in units of \hbar . In the present experiment, $\bar{\ell} \approx 6 \times 10^3$ and $\sigma_{\ell} \approx 20$. The corresponding mean rotation frequency, $\omega_{\text{rot}} = 2\omega_r \bar{\ell}$, is chosen to be between 142 and 149 kHz. This procedure yields resolved sidebands on the $|S\rangle \leftrightarrow |D\rangle$ 729 nm transition at frequencies $\Delta\ell\omega_{\text{rot}}$ for integer $\Delta\ell$, corresponding to rotational state transitions $|\ell\rangle \rightarrow |\ell + \Delta\ell\rangle$. This allows selection of well-defined angular momentum changes $\Delta\ell$ by tuning the frequency of the 729 nm laser to the corresponding sideband frequency.

To determine the angular momentum diffusion coefficient, we measure the width of the rotor state σ_{ℓ} over time as it interacts with the environment. This is done with a Ramsey experiment to measure the linewidth of the $\Delta\ell = 1$ sideband, which is equal to $4\omega_r \sigma_{\ell}$ [48]. This relation expresses the fact that a spread in angular momentum corresponds to an uncertainty in mean angular velocity, and thus also to a spread of transition frequencies on a given rotational sideband. The rotational sideband linewidth is thus a direct measure of σ_{ℓ} . One expects this width to increase with time as $\sigma_{\ell}(t_{\text{diff}}) = \sigma_{\ell}(0) + \sqrt{2D t_{\text{diff}}} / \hbar$. The measurement protocol is shown in Fig. 2a. After letting the rotor interact with the environment for time t_{diff} , we perform a Ramsey experiment on the $\Delta\ell = 1$ sideband. We add a small detuning of a few kHz to see Ramsey fringes, and extract the sideband linewidth directly from the fringe decay rate. For interaction with the engineered environment, we inject noise during the time between rotational state preparation and the Ramsey measurement. We find that the uncontrolled ambient environment induces diffusion coefficients between 2 and 20 \hbar^2/ms . Figure 2b shows a sample diffusion measurement of the engineered environment. In Fig. 2c, we plot the measured diffusion coefficient for noise spectral densities with varying center frequency. We find that the measured diffusion coefficient is maximized when the injected noise resonance is equal to $2\omega_{\text{rot}}$, and is consistent with a Lorentzian line-shape with bandwidth of 19 kHz as the center frequency of the noise is swept. Measured diffusion coefficients below $20 \hbar^2/\text{ms}$ are likely prevented here by ambient noise.

To verify that the angular momentum diffusion is accompanied by decoherence, a direct coherence measurement is required. For this, we perform a Ramsey experiment on a chosen $\Delta\ell$ sideband in the presence of the noise bath. The initial $\pi/2$ pulse applies the operation $|SS, \ell\rangle \rightarrow$

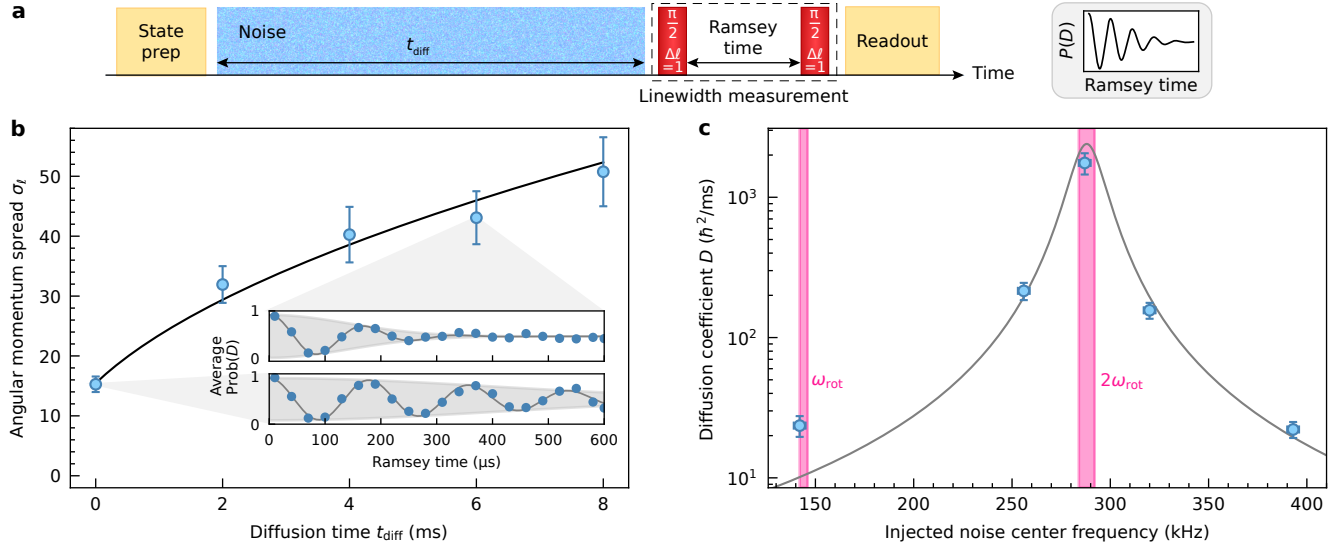


Fig. 2. Measurements of the angular momentum diffusion coefficient. **a**, Diagram of the measurement protocol for the angular momentum spread. A rotating coherent state is prepared, and noise is injected for a time t_{diff} . Afterward, the linewidth of the $\Delta\ell = 1$ sideband is measured with a Ramsey experiment. **b**, A sample diffusion coefficient measurement. Angular momentum distribution width σ_ℓ is measured as a function of time after rotational state preparation, with a constant level of noise injected during the diffusion time. The solid line is a fit giving $D = 156(20) \hbar^2/\text{ms}$. Inset: Selected individual Ramsey measurements of σ_ℓ with a detuning of 6 kHz from the $\Delta\ell = 1$ sideband transition. The y -axis is the average probability of an ion to be found in the $|D\rangle$ state. The shaded region shows the inferred phase contrast from the data, from which σ_ℓ is inferred. **c**, Demonstration of the $2\omega_{\text{rot}}$ resonance. Diffusion is measured at a rotation frequency $\omega_{\text{rot}} = 144(2)$ kHz. For each data point, the center frequency of the injected noise spectrum is shifted, while the amplitude and bandwidth are preserved, and the rotation frequency is kept constant. A Lorentzian lineshape, centered at $2\omega_{\text{rot}}$ and with bandwidth equal to the injected noise bandwidth of 19 kHz, is shown for reference. Vertical bands are at ω_{rot} and $2\omega_{\text{rot}}$ including variation.

$(|SS, \ell\rangle \pm |SD, \ell+\Delta\ell\rangle - |DS, \ell+\Delta\ell\rangle \mp |DD, \ell+2\Delta\ell\rangle)/2$, where the signs depend on whether $\Delta\ell$ is odd (top) or even (bottom). Subsequent coherent evolution results in a dephasing of the electronic state on the 100 μs timescale due to the spread in angular momentum space of the initial state and the nonlinearity of the rotor spectrum [48]. We therefore add a Hahn echo pulse to the center of the Ramsey scheme to compensate for this by reversing the free evolution. The interferometer is closed by a final $\pi/2$ pulse after time τ . With the echo pulse included, any measured loss in phase contrast can be attributed to nonunitary dynamics. For interaction with the engineered environment, we inject noise during the Ramsey evolution. The remaining coherence is quantified by the amplitude of the Ramsey fringe when the phase of the final pulse is scanned from 0 to 2π . We emphasize that this measurement is sensitive only to coherences between angular momentum states whose separation is exactly $\Delta\ell$, even in the presence of an initial state with $\sigma_\ell \gg 1$, due to the resolved $\Delta\ell$ sidebands of the electronic transition being addressed by the laser. We rule out other known potential decoherence mechanisms which could otherwise contribute to decay in fringe contrast by independent measurements (see Methods).

A sample of rotational decoherence measurements is

presented in Fig. 3a, which shows the Ramsey phase contrast C as a function of total Ramsey time τ for angular momentum superposition orders $\Delta\ell = 1, 2$, and 3. These measurements are each made with the same level of noise injection such that $D = 70 \hbar^2/\text{ms}$, as determined by an independent measurement of diffusion. Each is fit to the theoretical prediction $C(\tau) = C_0 \exp [-(\gamma\tau)^3]$ (see below), where C_0 is the phase contrast without rotational decoherence, which may be less than unity due to imperfect operations. We interpret the fitted parameter γ as the measured decoherence rate. The fitted decoherence rates from Fig. 3a are plotted against superposition order $\Delta\ell$ in the inset of Fig. 3b, and are fit to a power law. In Fig. 3b, we present similar triplets of decoherence rates for superpositions $\Delta\ell = 1, 2, 3$ across various strengths of the system-environment interaction, which are measured by the angular momentum diffusion coefficient. By varying the amplitude of injected noise, we tune the diffusion coefficient from $2.1 \hbar^2/\text{ms}$ (ambient environment, no noise injected) to $1000 \hbar^2/\text{ms}$. The solid curves are derived directly from the solution to the master equation with no free fitting parameters, as described next.

To understand our decoherence measurements theoretically, we approximately solve the master equation (1) between the initial $\pi/2$ and the Hahn echo pulse and

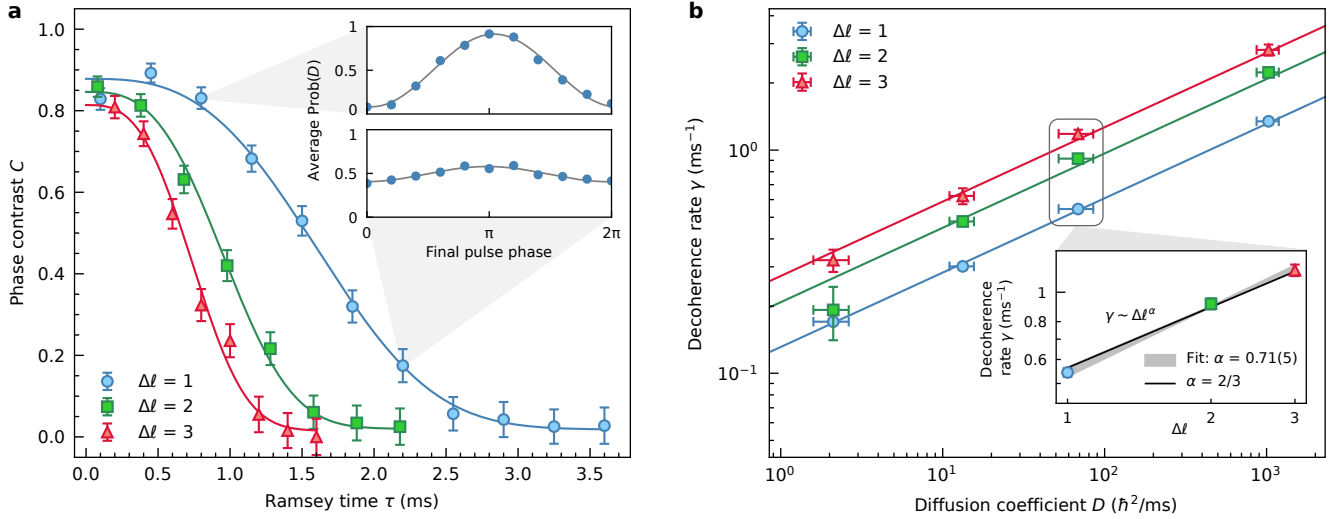


Fig. 3. Measurements of rotational decoherence. **a**, Sample measurements of the decay of phase contrast for superposition states with $\Delta\ell = 1, 2, 3$ at a constant level of noise injected such that $D = 70 \hbar^2/\text{ms}$. Inset: Selected individual phase scans for $\Delta\ell = 1$ using the pulse sequence shown in Fig. 1c. **b**, Decoherence rate measured against angular momentum diffusion coefficient. The leftmost datapoints are derived from an ambient environment where $D = 2.1 \hbar^2/\text{ms}$, and the others are obtained from use of the engineered environment, with varying amplitudes of injected noise. Solid curves are produced from Eq. (6), with no free fitting parameters. Inset: Decoherence rates, from the data points at $D = 70 \hbar^2/\text{ms}$ in the main plot, plotted against $\Delta\ell$ on a log-log scale. The shaded area shows a power law fit including uncertainty. The black line shows the theoretically expected power law of $\Delta\ell^{2/3}$ from Eq. (6).

again between the Hahn echo pulse and the final $\pi/2$ pulse with the initial state $|SS, \Psi_{\ell}\rangle$. The first $\pi/2$ pulse entangles the ion crystal's electronic state with the rotational state, creating superpositions of the ion crystal revolving at different angular velocities as determined by $\Delta\ell$. The resulting angular separation increases linearly in time until $\tau/2$, leading to a maximal instantaneous decoherence rate of $\sin^2(\omega_r \Delta\ell \tau)$. After the Hahn echo pulse, the angular separation decreases again until the interferometer is closed by the final $\pi/2$ pulse. We measure the decoherence rate via the decay of the Ramsey fringe contrast, which can be shown to be given by (see Methods)

$$C(\tau) = C_0 \exp \left(-\frac{D\tau}{2\hbar^2} [1 - \text{sinc}(2\omega_r \Delta\ell \tau)] \right). \quad (4)$$

This describes an exponential decay modulated with the rate of angular separation $2\omega_r \Delta\ell$. The experiment takes place in a regime where the angular frequency difference between the states $2\omega_r \Delta\ell$ is small compared to the diffusion coefficient: $2\omega_r \Delta\ell \ll D/\hbar^2$. In this regime, decoherence occurs well before the completion of the first oscillation at time $\tau = \pi/\omega_r \Delta\ell$. This restricts the angular separation to small angles. The decay profile (4) then reduces to

$$C(\tau) = C_0 \exp [-(\gamma\tau)^3], \quad (5)$$

with the rate

$$\gamma = \left(\frac{\omega_r^2 \Delta\ell^2 D}{3\hbar^2} \right)^{1/3}. \quad (6)$$

We experimentally confirm three important predictions from (5) and (6): (i) The shape of the contrast decay profile (5) matches the measured decay profile in Fig. 3a. In the picture of superposed time-dependent orientations, the τ^3 -dependence may be understood as the integral of an instantaneous decoherence rate that is quadratic in the angular separation. This is a signature of the sine-squared orientational scaling of rotational decoherence in the small-angle limit, since for small angular separation one obtains $\sin^2[\phi(t) - \phi'(t)] = \sin^2(2\omega_r \Delta\ell t) \approx (2\omega_r \Delta\ell t)^2$. (ii) The power-law scaling for the decoherence rate (6) with $\Delta\ell$, $\gamma \sim \Delta\ell^{2/3}$, is confirmed by the fit in the inset of Fig. 3b. This yields $\gamma \sim \Delta\ell^{0.71(5)}$, which is consistent with the expected scaling. Repeating this analysis for the four diffusion coefficients in the main plot of Fig. 3b and averaging the exponents, we find $\gamma \sim \Delta\ell^{0.65(4)}$. As with the shape of the coherence profile in time, the scaling $\gamma \sim \Delta\ell^{2/3}$ also results directly from the sine-squared orientational scaling, since $\Delta\ell$ sets the speed of angular separation. (iii) The power-law scaling of the decoherence rate (6) with diffusion coefficient, $\gamma \sim D^{1/3}$, can be seen in our measurements in Fig. 3b, where the slope of the solid curves follows this $1/3$ power law. We emphasize that the solid curves come directly from (6) with no free parameters. Thus in addition to finding agreement with all expected scalings of

the rotational decoherence process, we also find that the absolute values of the measured decoherence rates agree with predictions from the master equation. We see agreement over the full range of diffusion coefficients, spanning nearly three orders of magnitude.

In summary, we have presented a systematic experimental study of the decoherence dynamics of a trapped-ion planar rotor due to a noisy electric field. We have verified the theoretical prediction that the decoherence rate of a superposition of two orientations is proportional to $\sin^2(\phi - \phi')$. In addition, by independently engineering and measuring the rate of angular momentum diffusion, we have confirmed the dependence of rotational decoherence on angular momentum diffusion. These results serve as a controlled, systematic test of the theory of rotor de-

coherence.

There are several ways to extend what we have demonstrated in the near term and probe further aspects of rotor decoherence. Extending the present work to more complicated rotors, containing for instance three or more ions revolving at fixed distances in a plane, would enable the observation of decoherence-free subspaces in the rotational degree of freedom [45]. In addition, correlating the observed rotational heating with heating of the rotor's center-of-mass motion and rocking motion may enable systematic studies of surface noise that go beyond heating measurements with single ions [46]. In the long term, this work constitutes a necessary step towards utilizing rotational quantum coherence for sensing, quantum information processing, and fundamental tests [14, 19–26].

[1] C. P. Koch, M. Lemeshko, and D. Sugny, *Reviews of Modern Physics* **91**, 035005 (2019).

[2] C. W. Chou, A. L. Collopy, C. Kurz, Y. Lin, M. E. Hardig, P. N. Plessow, T. Fortier, S. Diddams, D. Leibfried, and D. R. Leibrandt, *Science* **367**, 1458 (2020).

[3] Y. Lin, D. R. Leibrandt, D. Leibfried, and C.-w. Chou, *Nature* **581**, 273 (2020).

[4] M. Sinhal, Z. Meir, K. Najafian, G. Hegi, and S. Willitsch, *Science* **367**, 1213 (2020).

[5] K. K. Voges, P. Gersema, M. Meyer zum Alten Borgloh, T. A. Schulze, T. Hartmann, A. Zenesini, and S. Ospelkaus, *Physical Review Letters* **125**, 083401 (2020).

[6] A. Schindewolf, R. Bause, X.-Y. Chen, M. Duda, T. Karman, I. Bloch, and X.-Y. Luo, *Nature* **607**, 677 (2022).

[7] I. Stevenson, A. Z. Lam, N. Bigagli, C. Warner, W. Yuan, S. Zhang, and S. Will, *Physical Review Letters* **130**, 113002 (2023).

[8] B. Yan, S. A. Moses, B. Gadway, J. P. Covey, K. R. A. Hazzard, A. M. Rey, D. S. Jin, and J. Ye, *Nature* **501**, 521 (2013).

[9] Y. Bao, S. S. Yu, L. Anderegg, E. Chae, W. Ketterle, K.-K. Ni, and J. M. Doyle, “Dipolar spin-exchange and entanglement between molecules in an optical tweezer array,” (2022), arxiv:2211.09780 [physics, physics:quant-ph].

[10] L. Christakis, J. S. Rosenberg, R. Raj, S. Chi, A. Morningstar, D. A. Huse, Z. Z. Yan, and W. S. Bakr, *Nature* **614**, 64 (2023).

[11] J.-R. Li, K. Matsuda, C. Miller, A. N. Carroll, W. G. Tobias, J. S. Higgins, and J. Ye, *Nature* **614**, 70 (2023).

[12] P. D. Gregory, L. M. Fernley, A. L. Tao, S. L. Bromley, J. Stepp, Z. Zhang, S. Kotochigova, K. R. A. Hazzard, and S. L. Cornish, “Second-scale rotational coherence and dipolar interactions in a gas of ultracold polar molecules,” (2023), arxiv:2306.02991 [cond-mat, physics:physics].

[13] T. Delord, P. Huillery, L. Nicolas, and G. Hétet, *Nature* **580**, 56 (2020).

[14] J. Ahn, Z. Xu, J. Bang, P. Ju, X. Gao, and T. Li, *Nature Nanotechnology* **15**, 89 (2020).

[15] F. van der Laan, F. Tebbenjohanns, R. Reimann, J. Vijayan, L. Novotny, and M. Frimmer, *Physical Review Letters* **127**, 123605 (2021).

[16] B. A. Stickler, K. Hornberger, and M. S. Kim, *Nature Reviews Physics* **3**, 589 (2021).

[17] A. Pontin, H. Fu, M. Toroš, T. S. Monteiro, and P. F. Barker, *Nature Physics* **19**, 1003 (2023).

[18] M. Kamba, R. Shimizu, and K. Aikawa, “Nanoscale feedback control of six degrees of freedom of a near-sphere,” (2023), arxiv:2303.02831 [physics, physics:quant-ph].

[19] D. DeMille, *Physical Review Letters* **88**, 067901 (2002).

[20] A. L. Grimsmo, J. Combes, and B. Q. Baragiola, *Physical Review X* **10**, 011058 (2020).

[21] V. V. Albert, J. P. Covey, and J. Preskill, *Physical Review X* **10**, 031050 (2020).

[22] Y. L. Zhou, M. Ortner, and P. Rabl, *Physical Review A* **84**, 052332 (2011).

[23] W. Lechner and P. Zoller, *Physical Review Letters* **111**, 185306 (2013).

[24] B. Sundar, B. Gadway, and K. R. A. Hazzard, *Scientific Reports* **8**, 3422 (2018).

[25] B. A. Stickler, B. Papendell, S. Kuhn, B. Schrinski, J. Millen, M. Arndt, and K. Hornberger, *New Journal of Physics* **20**, 122001 (2018).

[26] Y. Ma, K. E. Khosla, B. A. Stickler, and M. S. Kim, *Physical Review Letters* **125**, 053604 (2020).

[27] T. Vieillard, F. Chaussard, D. Sugny, B. Lavorel, and O. Faucher, *Journal of Raman Spectroscopy* **39**, 694 (2008).

[28] N. Owschimikow, F. Königsmann, J. Maurer, P. Giese, A. Ott, B. Schmidt, and N. Schwentner, *Journal of Chemical Physics* **133**, 184302 (2010).

[29] A. A. Milner, A. Korobenko, J. W. Hepburn, and V. Milner, *Physical Review Letters* **113**, (2014).

[30] I. F. Tenney, M. Artamonov, T. Seideman, and P. H. Bucksbaum, *Physical Review A* **93**, 13421 (2016).

[31] R. Damari, D. Rosenberg, and S. Fleischer, *Physical Review Letters* **119**, 033002 (2017).

[32] B. Neyenhuis, B. Yan, S. A. Moses, J. P. Covey, A. Chotia, A. Petrov, S. Kotochigova, J. Ye, and D. S. Jin, *Physical Review Letters* **109**, 230403 (2012).

[33] F. Seeßelberg, X.-Y. Luo, M. Li, R. Bause, S. Kotochigova, I. Bloch, and C. Gohle, *Physical Review Letters* **121**, 253401 (2018).

[34] R. Bause, M. Li, A. Schindewolf, X.-Y. Chen, M. Duda, S. Kotochigova, I. Bloch, and X.-Y. Luo, *Physical Re-*

view Letters **125**, 023201 (2020).

[35] S. Burchesky, L. Anderegg, Y. Bao, S. S. Yu, E. Chae, W. Ketterle, K.-K. Ni, and J. M. Doyle, Physical Review Letters **127**, 123202 (2021).

[36] B. A. Stickler, B. Papendell, and K. Hornberger, Physical Review A **94**, (2016).

[37] C. Zhong and F. Robicheaux, Physical Review A **94**, 52109 (2016).

[38] B. Papendell, B. A. Stickler, and K. Hornberger, New Journal of Physics **19**, (2017).

[39] B. A. Stickler, B. Schrinski, and K. Hornberger, Physical Review Letters **121**, (2018).

[40] M. Schlosshauer, Physics Reports Quantum Decoherence, **831**, 1 (2019).

[41] D. Walls and G. Milburn, Physical Review A **31**, 2403 (1985).

[42] M. Brune, E. Hagley, J. Dreyer, X. Maître, A. Maali, C. Wunderlich, J. M. Raimond, and S. Haroche, Physical Review Letters **77**, 4887 (1996).

[43] C. J. Myatt, B. E. King, Q. A. Turchette, C. A. Sackett, D. Kielpinski, W. M. Itano, C. Monroe, and D. J. Wineland, Nature **403**, 269 (2000).

[44] A. Auffeves, P. Maioli, T. Meunier, S. Gleyzes, G. Nogues, M. Brune, J. M. Raimond, and S. Haroche, Physical Review Letters **91**, 230405 (2003).

[45] J. S. Pedernales, F. Cosco, and M. B. Plenio, Physical Review Letters **125**, 090501 (2020).

[46] L. Martinetz, K. Hornberger, and B. A. Stickler, PRX Quantum **3**, 030327 (2022).

[47] H.-K. Li, E. Urban, C. Noel, A. Chuang, Y. Xia, A. Ransford, B. Hemmerling, Y. Wang, T. Li, H. Häffner, and X. Zhang, Physical Review Letters **118**, 053001 (2017).

[48] E. Urban, N. Glikin, S. Mouradian, K. Krimmel, B. Hemmerling, and H. Häffner, Physical Review Letters **123**, 133202 (2019).

[49] M. Brownnutt, M. Kumph, P. Rabl, and R. Blatt, Reviews of Modern Physics **87**, 1419 (2015).

METHODS

Derivation of the master equation

We consider a planar rigid rotor formed by two ions with charges e at positions $r_{1,2} = z\mathbf{e}_z \pm r\mathbf{e}_\rho(\phi)$, where z is the height above the surface trap, $2r$ is the ion separation, and the angle ϕ describes the rotor orientation. The potential energy of the rotor in the quadrupole potential follows as

$$V_t(\phi) = -er^2 \mathbf{e}_\rho(\phi) \cdot [\nabla \otimes \mathbf{E}(z\mathbf{e}_z, t)] \mathbf{e}_\rho(\phi), \quad (7)$$

where $\mathbf{E}(\mathbf{r}, t)$ is the local field strength at time t . The vector gradient $\nabla \otimes \mathbf{E}(z\mathbf{e}_z, t)$ is symmetric, traceless, and determined by the trap geometry. Using $L_\pm = e^{\pm i\phi}$ the potential energy can be rewritten, up to an additive constant, as

$$V_t(\phi) = \frac{er^2}{4} (\varepsilon_t L_+^2 + \varepsilon_t^* L_-^2). \quad (8)$$

Here, we defined the complex-valued combination of field gradients

$$\varepsilon_t = -\partial_x E_x + \partial_y E_y + 2i\partial_x E_y, \quad (9)$$

whose magnitude is determined by the trapping geometry and the time-dependent voltage at the control electrodes.

The rotor quantum state $|\psi_t\rangle$ evolves according to the Schrödinger equation with Hamiltonian $H_0 + V_t(\phi)$, involving the kinetic energy $H_0 = L_z^2/2I$. Switching to the interaction picture $|\chi_t\rangle = \exp(iH_0t/\hbar)|\psi_t\rangle$ introduces the interaction picture potential $\exp(iH_0t/\hbar)V\exp(-iH_0t/\hbar)$, which can be evaluated by using that

$$e^{iH_0t/\hbar} L_\pm^2 e^{-iH_0t/\hbar} = e^{2i\hbar t/I} L_\pm^2 e^{\pm 2itL_z/I}, \quad (10)$$

as follows from the commutation relations $[L_z, L_\pm] = \pm\hbar L_\pm$ and unitarity, $L_\pm L_\mp = \mathbb{I}$. We consider a rapidly revolving rotor state $|\chi_t\rangle$ with mean angular momentum quantum number $\bar{\ell} = I\omega_{\text{rot}}/\hbar \gg 1$ much greater than the spread σ_ℓ . We can thus approximate $\exp(\pm 2itL_z/I)|\chi_t\rangle \simeq e^{\pm 2i\omega_{\text{rot}}t}|\chi_t\rangle$, yielding the interaction-picture Schrödinger equation $i\hbar\partial_t|\chi_t\rangle = \tilde{V}_t|\chi_t\rangle$ with

$$\tilde{V}_t = \frac{er^2}{4} (\varepsilon_t e^{2i\omega_{\text{rot}}t} L_+^2 + \varepsilon_t^* e^{-2i\omega_{\text{rot}}t} L_-^2). \quad (11)$$

Integrating this Schrödinger equation iteratively over the time interval $\Delta t \gg 1/\omega_{\text{rot}}$ yields an integral equation

$$|\chi_{t+\Delta t}\rangle = |\chi_t\rangle - \frac{i}{\hbar} \int_t^{t+\Delta t} dt' \tilde{V}_{t'} |\chi_t\rangle - \frac{1}{\hbar^2} \int_t^{t+\Delta t} dt' \int_t^{t'} dt'' \tilde{V}_{t'} \tilde{V}_{t''} |\chi_{t''}\rangle. \quad (12)$$

where we may approximate $|\chi_{t''}\rangle \simeq |\chi_t\rangle$ to express that $|\chi_t\rangle$ evolves little in Δt .

This equation describes how the dynamics of $|\chi_t\rangle$ is influenced by the random voltage noise applied to the control electrodes. Given that the rotor-surface distance is so short that field retardation can be neglected, the statistical properties the voltage noise directly translate to those of ε_t . In the ensemble average, the rotor state is then described by a Lindblad quantum master equation for the density operator $\tilde{\rho}$ (see Supplement),

$$\begin{aligned} \partial_t \tilde{\rho} &= \frac{1}{\Delta t} [\mathbb{E}(|\chi_{t+\Delta t}\rangle \langle \chi_{t+\Delta t}|) - |\chi_t\rangle \langle \chi_t|] \\ &\simeq \frac{D}{4\hbar^2} (L_+^2 \tilde{\rho} L_-^2 + L_-^2 \tilde{\rho} L_+^2 - 2\tilde{\rho}). \end{aligned} \quad (13)$$

Here, \mathbb{E} denotes the ensemble average over the stationary stochastic voltage process, and we defined the angular momentum diffusion coefficient (3) with the power spectral density

$$S_\varepsilon(\omega) = \int_{-\infty}^{\infty} d\tau \mathbb{E}(\varepsilon_t \varepsilon_{t-\tau}^*) e^{i\omega\tau}. \quad (14)$$

In Eq. (13) we used that Δt is large in comparison to the noise correlation time as determined by the noise filter bandwidth of 19 kHz. The latter is indeed much greater than the width of rotation frequencies $\sigma_\ell \hbar / I \simeq 1$ kHz. Transforming back to the Schrödinger picture yields (under the same assumptions as above) the master equation (1).

Decoherence of angular momentum superpositions

Driving the rotor state at a rotational sideband of angular momentum offset $\Delta\ell$ allows applying the $\pi/2$ pulse (see Supplement)

$$X_{\pi/2} = \frac{\mathbb{I}}{2} - \frac{\sigma_1^+ + (-1)^{\Delta\ell} \sigma_2^+}{2} L_+^{\Delta\ell} + \frac{\sigma_1^- + (-1)^{\Delta\ell} \sigma_2^-}{2} L_-^{\Delta\ell} + \frac{(-1)^{\Delta\ell}}{2} (\sigma_1^+ \sigma_2^+ L_+^{2\Delta\ell} + \sigma_1^- \sigma_2^- L_-^{2\Delta\ell} - \sigma_1^+ \sigma_2^- - \sigma_1^- \sigma_2^+). \quad (15)$$

and the π pulse

$$X_\pi = (-1)^{\Delta\ell} (\sigma_1^+ \sigma_2^+ L_+^{2\Delta\ell} + \sigma_1^- \sigma_2^- L_-^{2\Delta\ell} - \sigma_1^+ \sigma_2^- - \sigma_1^- \sigma_2^+). \quad (16)$$

Here, $\sigma_{1,2}^\pm$ are the raising/lowering operators for the electronic levels of the two ions. The pulses can be used to implement a Ramsey interference scheme involving the steps:

- (0) **Initialization**—The rotor is prepared in the coherent rotor state $|\Phi_0\rangle = |SS, \Psi_{\bar{\ell}}\rangle$ with mean angular momentum $\bar{\ell} \gg \sigma_\ell$.
- (1) **Creation of the superposition**—At $t = 0$, a $\pi/2$ pulse creates a superposition of angular momentum states $|\Phi_1\rangle = X_{\pi/2} |\Phi_0\rangle$. Direct application of Eq. (15) yields the threefold superposition

$$|\Phi_1\rangle = \frac{1}{2} (|1\rangle - \sqrt{2} |2\rangle + |3\rangle), \quad (17)$$

of the orthonormal states

$$|1\rangle = |SS, \Psi_{\bar{\ell}}\rangle \quad (18a)$$

$$|2\rangle = \frac{1}{\sqrt{2}} (|DS\rangle + (-1)^{\Delta\ell} |SD\rangle) |\Psi_{\bar{\ell}+\Delta\ell}\rangle \quad (18b)$$

$$|3\rangle = (-1)^{\Delta\ell} |DD, \Psi_{\bar{\ell}+2\Delta\ell}\rangle. \quad (18c)$$

The laser pulse thus entangles the two ion's internal state with that of the rotational degree of freedom. Whether $\Delta\ell$ is even or odd determines whether the $\pi/2$ pulse creates the even or odd superposition of $|DS\rangle$ and $|SD\rangle$.

- (2) **Time evolution**—This is followed by a evolution in presence of the stochastic potential (8) until $t = \tau/2$, $|\Phi_2\rangle = e^{-iH_{\text{rot}}\tau/2\hbar} U_{\tau/2} |\Phi_1\rangle$, where $H_{\text{rot}} = H_0 +$

$\hbar\Delta\omega(\sigma_1^+ \sigma_1^- + \sigma_2^+ \sigma_2^-)$ and $U_{\tau/2}$ describes the interaction picture time evolution in presence of a realisation of the stochastic potential with the laser-atom detuning $\Delta\omega$ (see Supplement).

- (3) **Hahn echo pulse**—At $t = \tau/2$, a π pulse implements a Hahn echo $|\Phi_3\rangle = X_\pi |\Phi_2\rangle$.
- (4) **Time evolution**—This is followed by a second time evolution in presence of the environment until $t = \tau$, $|\Phi_4\rangle = e^{-iH_{\text{rot}}\tau/2\hbar} U_{\tau/2} |\Phi_3\rangle$. Note that all states in this superposition are now translated by the same angle $2(\bar{\ell} + \Delta\ell)\omega_r\tau$, meaning that the interferometer can be closed.
- (5) **Closing of the interferometer**—A second $\pi/2$ pulse $|\Phi_5\rangle = X_{\pi/2} |\Phi_4\rangle$ closes the interferometer.
- (6) **Measurement**—Measuring the mean fluorescence light of the two atoms yields the mean probability of being in the excited state,

$$P(D) = \frac{1}{2} + \frac{1}{2} [\text{Prob}(DD) - \text{Prob}(SS)]. \quad (19)$$

Using the final state $|\Phi_5\rangle$ and averaging over many repetitions of the experiment yields (see Supplement)

$$P(D) = \frac{1}{2} - \frac{1}{2} \cos(\omega_r \Delta\ell^2 \tau) C(\tau), \quad (20)$$

with the reduction factor of the Ramsey fringe contrast (4).

Coherent effects on the contrast decay profile

From (20) we see that the phase contrast, which decays from decoherence as $C(\tau)$ given by (4), is additionally modulated by a factor

$$C_{\text{mod}}(\tau) = \cos(\omega_r \Delta\ell^2 \tau). \quad (21)$$

This arises from interference between the two relevant coherences of the rotor state: $|\ell\rangle \leftrightarrow |\ell + \Delta\ell\rangle$ and $|\ell + \Delta\ell\rangle \leftrightarrow |\ell + 2\Delta\ell\rangle$, whose respective transition frequencies differ by $2\Delta\ell^2\omega_r = 2\pi \times 26 \text{ Hz} \times \Delta\ell^2$. This modulation is necessarily present in the coherence measurements presented in this work, which otherwise yield a contrast profile of the form $\exp[-(\gamma\tau)^3]$. Equation (21) predicts a node in the fringe contrast at $\tau = \pi/(2\Delta\ell^2\omega_r)$. The modulation may therefore be safely neglected only if the coherence time is much shorter than the node time, $1/\gamma \ll \pi/(2\Delta\ell^2\omega_r)$. Otherwise, the effect of the modulation may be measurable before decoherence has occurred, and thus this effect must be accounted for in order to accurately estimate γ from the measurements. We find from numerical simulations that the modulation profile may be appreciably influenced by imperfect operations, where only a partial initial coherence is created, which we therefore must also take into account. Including corrections due to imperfect operations, the contrast node

is expected to occur at $\tau = 19$ ms for $\Delta\ell = 1$ superpositions, at 4.8 ms for $\Delta\ell = 2$, and at 2.4 ms for $\Delta\ell = 3$. For most of our measurements, this effect is negligible. In estimating the decoherence rate γ in Fig. 3b, we explicitly account for this effect only when $\Delta\ell^2\omega_r/2\pi\gamma > 0.1$. See Extended Data Fig. 1 for a demonstration of this effect.

Non-rigid effects

In the main text, we approximate the ion crystal as a rigid rotor. The leading-order non-rigid effect is centrifugal distortion: the moment of inertia increases as the square of the rotation frequency due to centrifugal force, effectively reducing the rotational constant ω_r with increasing angular momentum. For an in-plane confinement strength such that the center-of-mass vibrational frequency is ω_x , the fractional change to ω_r due to finite rotation frequency ω_{rot} is given by $2\omega_{\text{rot}}^2/\omega_x^2 = 2.0 \times 10^{-2}$ for parameters used in this work. This quantity is smaller than the fractional uncertainty of any measurement presented, so we neglect this correction.

Measurements of rotational friction

A finite-temperature environment interacting with a quantum rotor will have a frictional effect in addition to angular momentum diffusion, which in general may affect the decoherence dynamics [39]. We thus verify that the environment is well-approximated as infinite temperature by ascertaining that rotational friction is negligible. We measure rotational friction by recording the center frequency of a rotational sideband at various wait times after rotational state preparation. For increased sensitivity, the third rotational sideband frequency $\omega_{sb}^{(\Delta\ell=3)}$ is chosen, and the rotation frequency inferred as $\omega_{\text{rot}} = \omega_{sb}^{(\Delta\ell=3)}/3$. We do this for both an ambient environment ($D = 19 \text{ \AA}^2/\text{ms}$) and an engineered environment ($D = 110 \text{ \AA}^2/\text{ms}$). In both cases, we find the rate of slowdown to be consistent with zero. In the case of the ambient environment, we bound the rate of slowdown (2σ uncertainty of the slope of the fit) at $< 0.2 \text{ \AA}/\text{ms}$ in the case of the ambient environment, and $< 0.3 \text{ \AA}/\text{ms}$ in the case of the engineered environment. We thus ne-

glect rotational friction in the theoretical treatment in the main text. See Extended Data Fig. 2 for these measurements.

Additional decoherence sources

Two other potentially relevant effects are decoherence of the ions' electronic state and changes of the rotor's moment of inertia due to fluctuations of the trap frequency. We rule out both of these as significant contributions.

Since the Ramsey experiment entangles the angular momentum state of the rotor with the electronic state of the ions, decoherence of the electronic states will also result in a loss of measured phase contrast. To measure the electronic coherence time, we trap a single ion and prepare it in the superposition $|S\rangle + |D\rangle$ with a Ramsey experiment including a Hahn echo pulse. We find the $1/e$ coherence time to be 38 ms (see Extended Data Fig. 3), much longer than any coherence measurement presented in this work.

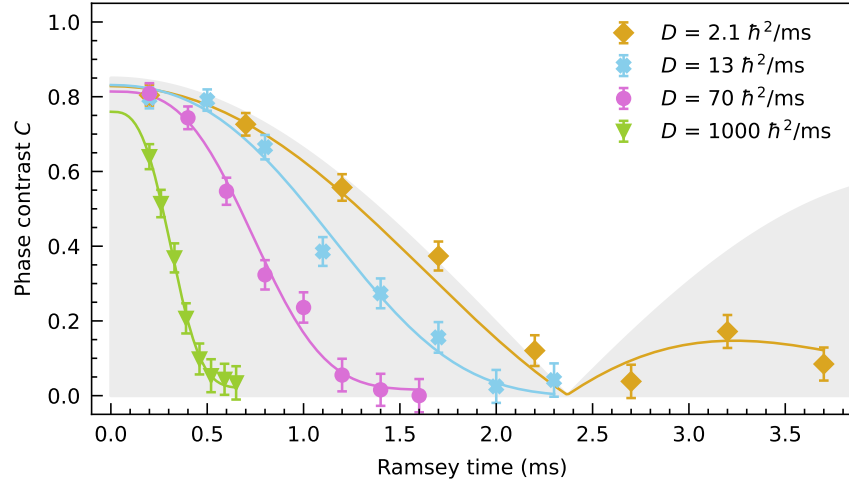
Changes in the rotor's moment of inertia conserve its angular momentum but change the rotation frequency, thereby also decohering a superposition of angular displacements. The stability of the moment of inertia I is determined by the stability of the transverse trap frequency ω_x , related by $I \propto \omega_x^{-4/3}$. We measure the stability of the trap frequency by trapping a single ion and preparing it in the Fock-state superposition $|0\rangle + |1\rangle$ with a Ramsey experiment including a Hahn echo pulse. We find a $1/e$ coherence time of 32 ms (see Extended Data Fig. 3). When propagated to the case of angular momentum superpositions in the rotor for $\omega_{\text{rot}} = 145 \text{ kHz}$, this yields an inferred rotational coherence time of $240 \text{ ms}/\Delta\ell$, again much longer than the coherence measurements presented.

Acknowledgements

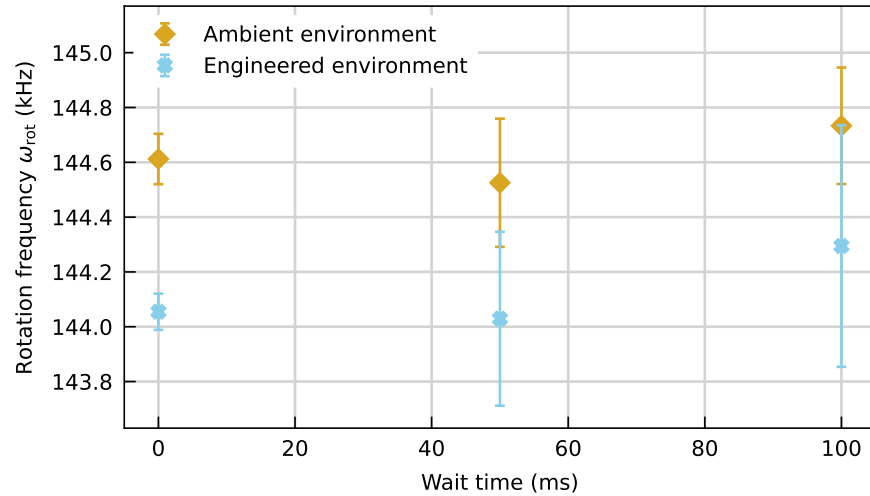
Funding provided by the NSF Grant No. PHY 2011973 and by AFOSR Grant No. FA9550-23-1-0546.

B.A.S. acknowledges support by the Deutsche Forschungsgemeinschaft (DFG, German Research Foundation) – 510794108.

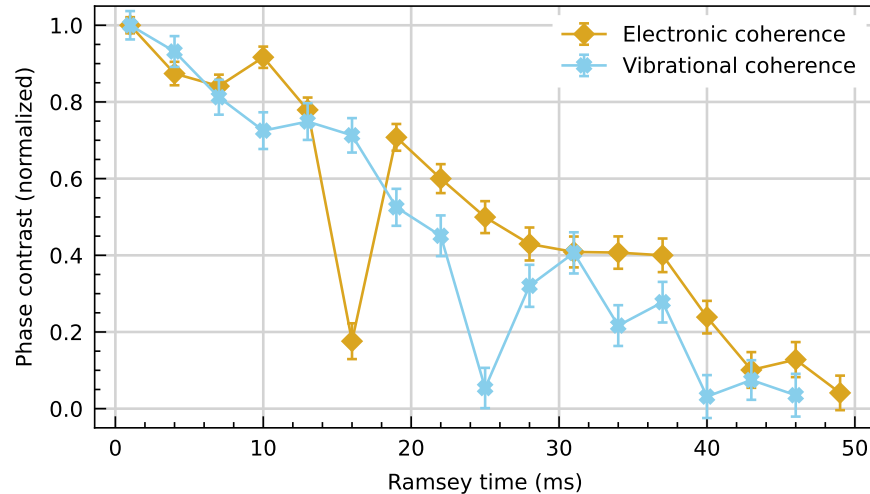
EXTENDED DATA FIGURES



Extended Data Fig. 1. **Coherent oscillations of phase contrast amplitude.** All contrast decay measurements for $\Delta\ell = 3$ measurements of decoherence presented in Fig. 3b are shown here. The shaded region is the contrast profile from coherent 4-level dynamics, modified from (21) to account for imperfect operations (sub-unity initial contrast) such that it yields agreement with numerical simulations (see Methods). Solid lines are fits of the form (5), additionally multiplied by the shaded profile in cases where $\Delta\ell^2\omega_r/2\pi\gamma > 0.1$, which here are $D = 2.1 \hbar^2/\text{ms}$ and $D = 13 \hbar^2/\text{ms}$.



Extended Data Fig. 2. **Measurements of rotational friction.** The rotation frequency is measured as a function of wait time after preparation of a rapidly rotating state, both without (without $D = 19 \hbar^2/\text{ms}$) and with ($D = 110 \hbar^2/\text{ms}$) voltage noise injection. Over 100 ms, no measurable slowdown is observed.



Extended Data Fig. 3. **Other coherence measurements.** Measurements of the electronic degree of freedom and the single-ion transverse vibrational degree of freedom are shown. Electronic coherence is measured using a single ion placed in the superposition $|S\rangle + |D\rangle$. A vibrational coherence measurement of the $|0\rangle + |1\rangle$ Fock state superposition probes the coherence of the transverse vibrational motion of a single ion, placing a limit on the stability of the rotor's moment of inertia. A Hahn echo pulse is included in both of these measurements to match the conditions of the rotational decoherence measurements.

Supplementary notes: Observation of rotational decoherence in a trapped-ion planar rotor

Neil Glikin,^{1,2} Benjamin A. Stickler,³ Ryan Tollefson,^{1,2} Sara Mouradian,⁴ Neha Yadav,^{1,2} Erik Urban,^{1,*} Klaus Hornberger,⁵ and Hartmut Haeffner^{1,2}

¹*Department of Physics, University of California, Berkeley, Berkeley, California 94720, USA*

²*Challenge Institute for Quantum Computation, University of California, Berkeley, Berkeley, California 94720, USA*

³*Institute for Complex Quantum Systems, Ulm University, Albert-Einstein-Allee 11, 89069 Ulm, Germany*

⁴*Department of Electrical and Computer Engineering,*

University of Washington, Seattle, Washington 98195, USA

⁵*University of Duisburg-Essen, Faculty of Physics, Lotharstraße 1, 47057 Duisburg, Germany*

This text provides further details on the theoretical description of the experiment.

I. DERIVATION OF THE MASTER EQUATION

We consider a planar rigid rotor formed by two ions with charges e at positions $r_{1,2} = z\mathbf{e}_z \pm r\mathbf{e}_\rho(\phi)$, where z is the height above the surface trap, $2r$ is the ion separation, and the angle ϕ describes the rotor orientation. The potential energy of the rotor in the quadrupole potential follows as

$$V(\phi) = -er^2 \mathbf{e}_\rho(\phi) \cdot [\nabla \otimes \mathbf{E}(z\mathbf{e}_z, t)] \mathbf{e}_\rho(\phi), \quad (\text{S1})$$

where $\mathbf{E}(\mathbf{r}, t)$ is the local field strength at time t . The vector gradient $\nabla \otimes \mathbf{E}(z\mathbf{e}_z, t)$ is symmetric and traceless, and determined by the trap geometry. Using that $L_\pm = e^{\pm i\phi}$, this potential energy can be rewritten up to an additive constant as

$$V_t(\phi) = \frac{er^2}{4} (\varepsilon_t L_+^2 + \varepsilon_t^* L_-^2), \quad (\text{S2})$$

where we defined the complex-valued combination of field gradients

$$\varepsilon_t = -\partial_x E_x + \partial_y E_y + 2i\partial_x E_y, \quad (\text{S3})$$

whose magnitude is determined by the trapping geometry as well as the time-dependent voltage applied to the control electrodes.

The quantum state $|\psi_t\rangle$ of the rotor evolves according to the Schrödinger equation with the free Hamiltonian $H_0 = L_z^2/2I$ and the potential (S2). Transformation to the interaction picture $|\psi_t\rangle = \exp(-iH_0t/\hbar)|\chi_t\rangle$ shows that the rotor evolves according to the interaction picture potential $\tilde{V}_t = \exp(iH_0t/\hbar)V_t \exp(-iH_0t/\hbar)$, which can be further evaluated by using that

$$L_\pm^2(t) = e^{iH_0t/\hbar} L_\pm^2 e^{-iH_0t/\hbar} = e^{2iht/I} L_\pm^2 e^{\pm 2itL_z/I}, \quad (\text{S4})$$

as follows from the commutation relations $[L_z, L_\pm] = \pm\hbar L_\pm$ and $L_\pm L_\mp = \mathbb{I}$. The interaction picture

Schrödinger equation is thus given by $i\hbar\partial_t |\chi_t\rangle = \tilde{V}_t |\chi_t\rangle$ with

$$\tilde{V}_t = \frac{er^2}{4} (e^{2iht/I} \varepsilon_t L_+^2 e^{2itL_z/I} + \text{h.c.}) . \quad (\text{S5})$$

We now integrate this Schrödinger equation over the time interval $\Delta t \gg 1/\omega_{\text{rot}}$ and iterate the resulting integral equation twice to obtain

$$|\chi_{t+\Delta t}\rangle = |\chi_t\rangle - \frac{i}{\hbar} \int_t^{t+\Delta t} dt' \tilde{V}_{t'} |\chi_t\rangle - \frac{1}{\hbar^2} \int_t^{t+\Delta t} dt' \int_t^{t'} dt'' \tilde{V}_{t'} \tilde{V}_{t''} |\chi_{t''}\rangle . \quad (\text{S6})$$

To express that $|\chi_t\rangle$ evolves little in Δt , we approximate $|\chi_{t''}\rangle \simeq |\chi_t\rangle$.

This equation describes how the dynamics of the pure state $|\chi_t\rangle$ is influenced by the time-dependent voltage applied to the control electrodes. This voltage is chosen randomly, so that the rotor state is described by the density operator $\tilde{\rho} = \mathbb{E}[|\chi_t\rangle \langle \chi_t|]$, where \mathbb{E} denotes the ensemble average over many repetitions of the experiment. The equation of motion for $\tilde{\rho}$ can be derived by calculating

$$\Delta\tilde{\rho} = \mathbb{E}(|\chi_{t+\Delta t}\rangle \langle \chi_{t+\Delta t}|) - |\chi_t\rangle \langle \chi_t| \quad (\text{S7})$$

by inserting Eq. (S6), which yields

$$\Delta\tilde{\rho} = \frac{1}{\hbar^2} \int_t^{t+\Delta t} dt' \int_t^{t+\Delta t} dt'' \mathbb{E} (\tilde{V}_{t'} \tilde{\rho} \tilde{V}_{t''}) - \frac{1}{\hbar^2} \int_t^{t+\Delta t} dt' \int_t^{t'} dt'' \left\{ \mathbb{E} (\tilde{V}_{t'} \tilde{V}_{t''}), \tilde{\rho} \right\} . \quad (\text{S8})$$

Here, $\{A, B\} = AB + BA$ denotes the anticommutator.

The time integrals appearing in Eq. (S8) can be calculated for rapidly revolving rotor states $|\chi_t\rangle$, which are localized in angular momentum close to the quantum number $\bar{\ell} = I\omega_{\text{rot}}/\hbar \gg 1$ with angular momentum spread $\sigma_\ell \ll \bar{\ell}$. Since this implies $\exp(\pm 2itL_z/I)|\chi_t\rangle \simeq e^{\pm 2i\omega_{\text{rot}}t}|\chi_t\rangle$ one is left with the integrals

$$\int_t^{t+\Delta t} dt' \int_t^{t+\Delta t} dt'' \mathbb{E} (\varepsilon_{t'} \varepsilon_{t''}^*) e^{2i\omega_{\text{rot}}(t'-t'')} \simeq \Delta t S_\varepsilon(2\omega_{\text{rot}}) \quad (\text{S9a})$$

* Current address: Exponent, Inc., Electrical Engineering and Computer Science Practice, Warrenville, IL

and

$$\int_t^{t+\Delta t} dt' \int_t^{t'} dt'' \mathbb{E}(\varepsilon_t \varepsilon_{t''}^*) e^{2i\omega_{\text{rot}}(t'-t'')} \simeq \frac{\Delta t}{2} S_\varepsilon(2\omega_{\text{rot}}) \quad (\text{S9b})$$

upon inserting (S5) and neglecting rapidly rotating terms $\exp[\pm i2\omega_{\text{rot}}(t'+t'')] \simeq 0$ in the rotating-wave approximation. In both integrals we used that ε_t is described by a real, stationary, and time-inversion-invariant stochastic process with zero mean, multiplied by a fixed complex phase factor (as determined by (S3)), to identify the power spectral density

$$S_\varepsilon(\omega) = \int_{-\infty}^{\infty} d\tau \mathbb{E}(\varepsilon_t \varepsilon_{t-\tau}^*) e^{i\omega\tau}. \quad (\text{S10})$$

The statistical properties of the applied voltage directly translate to those of ε_t since retardation effects in the field propagation can be neglected at the short distances of the experiment. The time interval Δt will be taken large compared to the decay time of the noise correlations. Moreover, the noise filter bandwidth of 20 kHz is large in comparison to the width of the rotation frequencies $\hbar\sigma_\ell/I \simeq 1$ kHz, justifying the approximation before Eq. (S9).

Inserting the integrals (S9) into equation (S8) shows that the ensemble-averaged quantum state follows the Markovian master equation

$$\partial_t \tilde{\rho} \simeq \frac{\Delta \tilde{\rho}}{\Delta t} = \frac{D}{4\hbar^2} (L_+^2 \tilde{\rho} L_-^2 + L_-^2 \tilde{\rho} L_+^2 - 2\tilde{\rho}), \quad (\text{S11})$$

with the diffusion coefficient given by Eq. (3) in the main text. Transforming back to the Schrödinger picture yields (under the same assumptions as above) the master equation (1).

II. TIME EVOLUTION IN THE NOISE FIELD

The time evolution under the master equation (1) can be determined by using Eq. (S6) for a pure state $|\chi_t\rangle$ and then calculating the ensemble average over many repetitions of the experiment. Specifically, approximating $|\chi_{t''}\rangle$ on the right hand side by $|\chi_t\rangle$ (see above), the operator

$$W(t) = \mathbb{I} - \frac{i}{\hbar} \int_t^{t+\Delta t} dt' \tilde{V}_{t'} - \frac{1}{\hbar^2} \int_t^{t+\Delta t} dt' \int_t^{t'} dt'' \tilde{V}_{t'} \tilde{V}_{t''} \quad (\text{S12})$$

propagates the state over the time interval Δt , $|\chi_{t+\Delta t}\rangle = W(t)|\chi_t\rangle$. Concatenating $N = t/\Delta t \gg 1$ of these timesteps, we can express the Schrödinger-picture state at time t as

$$|\psi_t\rangle = e^{-iH_0 t/\hbar} U_t |\psi_0\rangle, \quad (\text{S13})$$

where $|\psi_0\rangle$ is the initial state and

$$U_t \simeq W(t - \Delta t) \cdots W(\Delta t) W(0), \quad (\text{S14})$$

When calculating expectation values in the ensemble average, we can use that the random fields ε_t are uncorrelated between different time intervals $[n\Delta t, (n+1)\Delta t]$. One can thus decompose the ensemble average over the random noise trajectory $\mathbb{E}(\cdot)$ by the product of ensemble averages $\mathbb{E}_n(\cdot)$ at fixed times $t_n = n\Delta t$, so that

$$\mathbb{E}(\cdot) = \lim_{N \rightarrow \infty} \mathbb{E}_{N-1}(\mathbb{E}_{N-2}(\cdots \mathbb{E}_0(\cdot))). \quad (\text{S15})$$

This property will be used below to determine the outcome of the Ramsey interference protocol.

The Ramsey scheme discussed below requires the time evolution (S13) of a coherent rotor state $|\Psi_\ell\rangle$ characterized by a mean angular momentum quantum number ℓ and width σ_ℓ with $\ell \gg \sigma_\ell \gg 1$. Using that $L_\pm^2(t)|\Psi_\ell\rangle \simeq e^{\pm 4i\ell\omega_r t}|\Psi_\ell\rangle$, with $\omega_r = \hbar/2I$, yields

$$|\psi_t\rangle \simeq u_\ell(t) e^{-iH_0 t/\hbar} |\Psi_\ell\rangle \simeq u_\ell(t) e^{i\ell^2\omega_r t} e^{-i2\ell\omega_r t L_z/\hbar} |\Psi_\ell\rangle. \quad (\text{S16})$$

Here, $u_\ell(t)$ is the c-number obtained by replacing in U_t all operators $L_\pm^2(t_n)$ by $\exp(\pm 4i\ell\omega_r t_n)$. In the second expression, the unitary operator $\exp(-i2\ell\omega_r t L_z/\hbar)$ serves to displace the rotor state by the angle $2\ell\omega_r t$, while the global phase factor results from neglecting dispersion.

The Ramsey scheme also requires a generalization of (S16) for the case of a coherent rotor state displaced by the angle φ . Using that

$$L_\pm^2(t) e^{-i\varphi L_z/\hbar} = e^{\pm 2i\varphi} e^{-i\varphi L_z/\hbar} L_\pm^2(t), \quad (\text{S17})$$

we obtain

$$|\psi_t\rangle \simeq u_\ell(t|\varphi) e^{-iH_0 t/\hbar} e^{-i\varphi L_z/\hbar} |\Psi_\ell\rangle \simeq u_\ell(t|\varphi) e^{i\ell^2\omega_r t} e^{-i(\varphi + 2\ell\omega_r t) L_z/\hbar} |\Psi_\ell\rangle. \quad (\text{S18})$$

Like above, the c-numbers $u_\ell(t|\varphi)$ are obtained by replacing in U_t all operators $L_\pm^2(t_n)$ by $\exp[\pm 2i(\varphi + 2\ell\omega_r t_n)]$.

III. RABI PULSES

This section derives the action of a Rabi pulse on the four internal levels and the rotational degrees of freedom of the two-ion rotor. We start with the light-matter Hamiltonian

$$H_L = \sum_{j=1}^2 \sigma_j^+ f_L(\mathbf{r}_j, t) + \text{h.c.}, \quad (\text{S19})$$

where $\sigma_j^+ = |D\rangle_j \langle S|_j$ describes the excitation of the quadrupole transition of atom j , and $f_L(\mathbf{r}_j, t)$ is determined by the relevant field gradient at the position of the j -th atom. Assuming plane-wave illumination with inclination θ to the rotor plane, we have

$$f_L(\mathbf{r}_j, t) = \hbar g_0 e^{-i(kz \cos \theta + \omega t)} e^{i(-1)^j kr \sin \theta \cos \phi}, \quad (\text{S20})$$

where g_0 is the coupling rate, ω is the laser frequency, and $k = \omega/c$. Using that

$$\langle \ell + \Delta\ell | e^{\pm ikr \cos \theta \cos \phi} | \ell \rangle = (\pm i)^{\Delta\ell} J_{\Delta\ell}(kr \sin \theta), \quad (\text{S21})$$

one obtains

$$H_L = \hbar g_0 e^{-i(kz \cos \theta + \omega t)} \sum_{j=1}^2 \sum_{\Delta\ell \in \mathbb{Z}} (-1)^j i^{\Delta\ell} J_{\Delta\ell}(kr \sin \theta) \times J_{\Delta\ell}(kr \sin \theta) \sigma_1^+ L_+^{\Delta\ell} + \text{h.c.}, \quad (\text{S22})$$

The light-matter Hamiltonian (S22) can be further simplified by first transforming into the frame co-rotating with the laser field and then into the interaction picture with respect to $H_{\text{rot}} = \hbar \Delta\omega (\sigma_1^+ \sigma_1^- + \sigma_2^+ \sigma_2^-) + H_0$, where $\Delta\omega = \omega_0 - \omega$ denotes the laser detuning from the electronic transition frequency ω_0 . This yields

$$H_L(t) = e^{iH_{\text{rot}}t/\hbar} H_L e^{-iH_{\text{rot}}t/\hbar} = \hbar g_0 e^{-ikz \cos \theta} \sum_{j=1}^2 \sum_{\ell \in \mathbb{Z}} \sum_{\Delta\ell \in \mathbb{Z}} (-1)^j i^{\Delta\ell} J_{\Delta\ell}(kr \sin \theta) \times e^{it[\Delta\omega + \Delta\ell(2\ell + \Delta\ell)\omega_r]} \sigma_j^+ |\ell + \Delta\ell\rangle \langle \ell| + \text{h.c.} \quad (\text{S23})$$

For rapidly rotating states, where $2\ell + \Delta\ell \simeq 2\ell$, the laser frequency is tuned in resonance with the angular momentum transition $\Delta\ell$ by choosing $\omega \simeq \omega_0 + 2\ell\omega_r\Delta\ell$, so that

$$H_L(t) \simeq \hbar g [\sigma_1^+ L_+^{\Delta\ell} + (-1)^{\Delta\ell} \sigma_2^+ L_+^{\Delta\ell}] + \text{h.c.}, \quad (\text{S24})$$

where we defined

$$g = g_0 e^{-ikz \cos \theta} (-i)^{\Delta\ell} J_{\Delta\ell}(kr \sin \theta). \quad (\text{S25})$$

The excitation of the atom's electronic state is thus accompanied by an angular momentum kick of strength $\Delta\ell$. Applying the laser field for a short time period t , as described by the unitary

$$U_L(t) = \exp [-it(\sigma_1^+ L_+^{\Delta\ell} + \text{h.c.})] \times \exp [-it(-1)^{\Delta\ell} (\sigma_2^+ L_+^{\Delta\ell} + \text{h.c.})], \quad (\text{S26})$$

gives rise to Rabi oscillations, which can be used to implement $\pi/2$ -pulses and π -pulses. Specifically, choosing $gt = -i\pi/4$ implements a $\pi/2$ -pulse,

$$X_{\pi/2} = \frac{\mathbb{I}}{2} - \frac{\sigma_1^+ + (-1)^{\Delta\ell} \sigma_2^+}{2} L_+^{\Delta\ell} + \frac{\sigma_1^- + (-1)^{\Delta\ell} \sigma_2^-}{2} L_-^{\Delta\ell} + \frac{(-1)^{\Delta\ell}}{2} (\sigma_1^+ \sigma_2^+ L_+^{2\Delta\ell} + \sigma_1^- \sigma_2^- L_-^{2\Delta\ell} - \sigma_1^+ \sigma_2^- - \sigma_1^- \sigma_2^+). \quad (\text{S27})$$

Likewise, choosing $gt = -i\pi/2$ gives the π -pulse

$$X_\pi = (-1)^{\Delta\ell} (\sigma_1^+ \sigma_2^+ L_+^{2\Delta\ell} + \sigma_1^- \sigma_2^- L_-^{2\Delta\ell} - \sigma_1^+ \sigma_2^- - \sigma_1^- \sigma_2^+). \quad (\text{S28})$$

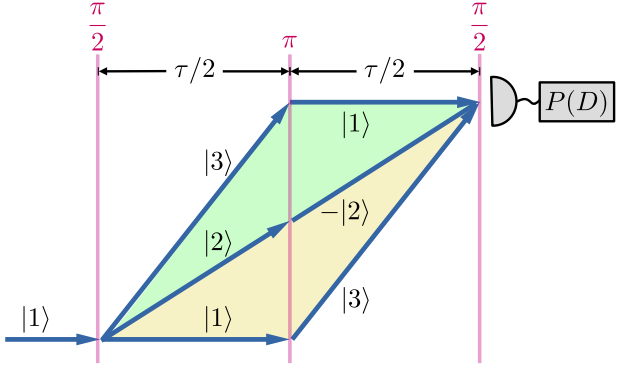


FIG. 1. Sketch of the rotational interferometer sequence consisting of the two $\pi/2$ -pulses and an intermediate π -pulse to implement a Hahn echo at separation $\tau/2$. The three involved two-ion rotor states, defined in Eqs. (S30), revolve with mean angular momentum $\bar{\ell}$, $\bar{\ell} + \Delta\ell$, and $\bar{\ell} + 2\Delta\ell$, respectively. The shaded regions indicate the coherences between superposition branches as read-out by the measurement of the mean excitation probability $P(D)$, see Eq. (S39).

IV. RAMSEY SCHEME

The interferometer sequence, as sketched in Fig. 1, consists of the following steps:

- (0) **Initialization**—The rotor is prepared in the coherent rotor state $|\Phi_0\rangle = |SS, \Psi_{\bar{\ell}}\rangle$ with mean angular momentum $\bar{\ell} \gg \sigma_\ell$.
- (1) **Creation of the superposition**—At $t = 0$, a $\pi/2$ -pulse creates a superposition of angular momentum states $|\Phi_1\rangle = X_{\pi/2} |\Phi_0\rangle$. Direct application of Eq. (S27) yields the threefold superposition

$$|\Phi_1\rangle = \frac{1}{2} (|1\rangle - \sqrt{2}|2\rangle + |3\rangle), \quad (\text{S29})$$

with the three orthonormal states

$$|1\rangle = |SS, \Psi_{\bar{\ell}}\rangle \quad (\text{S30a})$$

$$|2\rangle = \frac{1}{\sqrt{2}} (|DS\rangle + (-1)^{\Delta\ell} |SD\rangle) |\Psi_{\bar{\ell} + \Delta\ell}\rangle \quad (\text{S30b})$$

$$|3\rangle = (-1)^{\Delta\ell} |DD, \Psi_{\bar{\ell} + 2\Delta\ell}\rangle \quad (\text{S30c})$$

The laser pulse thus entangles the two ion's internal state with that of the rotational degree of freedom. Whether $\Delta\ell$ is even or odd determines whether the $\pi/2$ pulse creates the even or odd superposition of $|DS\rangle$ and $|SD\rangle$.

- (2) **Time evolution**—This is followed by a time evolution according to Eq. (S13) in presence of the environment until $t = \tau/2$, $|\Phi_2\rangle = e^{-iH_{\text{rot}}\tau/2\hbar} U_{\tau/2} |\Phi_1\rangle$. Using the result (S16) yields

$$|\Phi_2\rangle = \frac{1}{2} \left[a_{\bar{\ell}} T_{\bar{\ell}} |1\rangle - \sqrt{2} e^{-i\Delta\omega\tau/2} a_{\bar{\ell} + \Delta\ell} T_{\bar{\ell} + \Delta\ell} |2\rangle + e^{-i\Delta\omega\tau} a_{\bar{\ell} + 2\Delta\ell} T_{\bar{\ell} + 2\Delta\ell} |3\rangle \right]. \quad (\text{S31})$$

Here, we introduced the weights

$$a_\ell = e^{i\ell^2\omega_r\tau/2} u_\ell \left(\frac{\tau}{2} \right) \quad (\text{S32})$$

and the angular displacement operators

$$T_\ell = \exp \left(-i \frac{\ell \omega_r \tau L_z}{\hbar} \right) \quad (\text{S33})$$

(3) **Hahn echo pulse**—At $t = \tau/2$, a π -pulse implements a Hahn echo $|\Phi_3\rangle = X_\pi |\Phi_2\rangle$. Using Eq. (S28) this becomes

$$|\Phi_3\rangle = \frac{1}{2} \left[a_{\bar{\ell}} T_{\bar{\ell}} |3\rangle + e^{-i\Delta\omega\tau/2} \sqrt{2} a_{\bar{\ell}+\Delta\ell} T_{\bar{\ell}+\Delta\ell} |2\rangle + e^{-i\Delta\omega\tau} a_{\bar{\ell}+2\Delta\ell} T_{\bar{\ell}+2\Delta\ell} |1\rangle \right]. \quad (\text{S34})$$

(4) **Time evolution**—This is followed by the second time evolution in presence of the environment until $t = \tau$, $|\Phi_4\rangle = e^{-iH_{\text{rot}}\tau/2\hbar} U_{\tau/2} |\Phi_3\rangle$. Using Eq. (S18) yields

$$|\Phi_4\rangle = \frac{1}{2} e^{-i\Delta\omega\tau} T_{\bar{\ell}+\Delta\ell}^2 \left[b_{\bar{\ell}+2\Delta\ell}^{\bar{\ell}} a_{\bar{\ell}} |3\rangle + \sqrt{2} b_{\bar{\ell}+\Delta\ell}^{\bar{\ell}+\Delta\ell} a_{\bar{\ell}+\Delta\ell} |2\rangle + b_{\bar{\ell}}^{\bar{\ell}+2\Delta\ell} a_{\bar{\ell}+2\Delta\ell} |1\rangle \right], \quad (\text{S35})$$

where we abbreviated the weights

$$b_\ell^{\ell'} = e^{i\ell^2\omega_r\tau/2} u_\ell \left(\frac{\tau}{2} \right) | \omega_r \tau \ell' \rangle. \quad (\text{S36})$$

Note that all states in the superposition (S35) are translated by the same angle $2(\bar{\ell} + \Delta\ell)\omega_r\tau$, meaning that the interferometer can now be closed.

(5) **Closing of the interferometer**—A second $\pi/2$ -pulse $|\Phi_5\rangle = X_{\pi/2} |\Phi_4\rangle$ yields

$$|\Phi_5\rangle = \frac{1}{4} e^{-i\Delta\omega\tau} T_{\bar{\ell}+\Delta\ell}^2 \left[\sqrt{2} \left(b_{\bar{\ell}+2\Delta\ell}^{\bar{\ell}} a_{\bar{\ell}} - b_{\bar{\ell}}^{\bar{\ell}+2\Delta\ell} a_{\bar{\ell}+2\Delta\ell} \right) |2\rangle + \left(b_{\bar{\ell}+2\Delta\ell}^{\bar{\ell}} a_{\bar{\ell}} + 2b_{\bar{\ell}+\Delta\ell}^{\bar{\ell}+\Delta\ell} a_{\bar{\ell}+\Delta\ell} + b_{\bar{\ell}}^{\bar{\ell}+2\Delta\ell} a_{\bar{\ell}+2\Delta\ell} \right) |1\rangle + \left(b_{\bar{\ell}+2\Delta\ell}^{\bar{\ell}} a_{\bar{\ell}} - 2b_{\bar{\ell}+\Delta\ell}^{\bar{\ell}+\Delta\ell} a_{\bar{\ell}+\Delta\ell} + b_{\bar{\ell}}^{\bar{\ell}+2\Delta\ell} a_{\bar{\ell}+2\Delta\ell} \right) |3\rangle \right] \quad (\text{S37})$$

(6) **Measurement**—Measuring the mean fluorescence light of the two atoms yields the mean probability of being in the excited state,

$$\begin{aligned} P(D) &= \text{Prob}(DD) + \frac{1}{2} [\text{Prob}(DS) + \text{Prob}(SD)] \\ &= \frac{1}{2} + \frac{1}{2} [\text{Prob}(DD) - \text{Prob}(SS)]. \end{aligned} \quad (\text{S38})$$

Using the final state (S37) and averaging over many repetitions of the experiment yields

$$\begin{aligned} P(D) &= \frac{1}{2} - \frac{1}{4} \text{Re} \left[\mathbb{E} \left(b_{\bar{\ell}+\Delta\ell}^{\bar{\ell}+\Delta\ell} (b_{\bar{\ell}+2\Delta\ell}^{\bar{\ell}})^* \right) \mathbb{E}(a_{\bar{\ell}+\Delta\ell} a_{\bar{\ell}}^*) \right. \\ &\quad \left. + \mathbb{E} \left(b_{\bar{\ell}+\Delta\ell}^{\bar{\ell}+\Delta\ell} (b_{\bar{\ell}}^{\bar{\ell}+2\Delta\ell})^* \right) \mathbb{E}(a_{\bar{\ell}+\Delta\ell} a_{\bar{\ell}+2\Delta\ell}^*) \right]. \end{aligned} \quad (\text{S39})$$

Here, we used that the coefficients a_ℓ and $b_\ell^{\ell'}$ are statistically uncorrelated as discussed in the context of Eq. (S15). Next, we will explicitly calculate the ensemble averages in Eq. (S39).

V. ENSEMBLE AVERAGED SIGNAL

We are now in the position to evaluate the ensemble-averaged signal (S39) by using the decomposition (S14) and the rule (S15). We start with

$$\begin{aligned} \mathbb{E}(a_{\bar{\ell}+\Delta\ell} a_{\bar{\ell}}^*) &= \exp \left[i \frac{\omega_r \tau}{2} \Delta\ell (2\bar{\ell} + \Delta\ell) \right] \\ &\times \mathbb{E} \left[u_{\bar{\ell}+\Delta\ell} \left(\frac{\tau}{2} \right) u_{\bar{\ell}}^* \left(\frac{\tau}{2} \right) \right]. \end{aligned} \quad (\text{S40})$$

The expectation value in the second line can be calculated by writing

$$\mathbb{E} \left[u_{\bar{\ell}+\Delta\ell} \left(\frac{\tau}{2} \right) u_{\bar{\ell}}^* \left(\frac{\tau}{2} \right) \right] = \prod_{n,n'=0}^N \mathbb{E} [w_{\bar{\ell}+\Delta\ell}(n\Delta t) w_{\bar{\ell}}^*(n'\Delta t)], \quad (\text{S41})$$

where $\Delta t = \tau/2N$ with $N \gg 1$, and we defined

$$\begin{aligned} w_\ell(n\Delta t) &= 1 - \frac{i}{\hbar} \int_{n\Delta t}^{(n+1)\Delta t} dt' v_\ell(t') \\ &\quad - \frac{1}{\hbar^2} \int_{n\Delta t}^{(n+1)\Delta t} dt' \int_{n\Delta t}^{t'} dt'' v_\ell(t') v_\ell(t''), \end{aligned} \quad (\text{S42})$$

with

$$v_\ell(t) = \frac{er^2}{4} (\varepsilon_t e^{4i\ell\omega_r t} + \text{c.c.}) \quad (\text{S43})$$

This latter function is obtained by replacing $L_\pm^2(t)$ in the potential energy (S5) by the c-numbers $\exp(\pm 4i\ell\omega_r t)$.

Inserting Eq. (S42) into Eq. (S41) and using the same steps as in the derivation of the master equation yields

$$\begin{aligned} \mathbb{E} \left[u_{\bar{\ell}+\Delta\ell} \left(\frac{\tau}{2} \right) u_{\bar{\ell}}^* \left(\frac{\tau}{2} \right) \right] &\simeq \prod_{n=0}^N \left[1 - \frac{D\Delta t}{\hbar^2} \sin^2 [\Delta\ell (2n+1) \omega_r \Delta t] \right] \\ &\simeq \prod_{n=0}^N \exp \left[-\frac{D\Delta t}{\hbar^2} \sin^2 [\Delta\ell (2n+1) \omega_r \Delta t] \right]. \end{aligned} \quad (\text{S44})$$

For $N \gg 1$ the sum in the exponent can be approximated by an integral, leading to

$$\begin{aligned} \mathbb{E}(a_{\bar{\ell}+\Delta\ell} a_{\bar{\ell}}^*) &\simeq \exp \left(-\frac{D\tau}{4\hbar^2} [1 - \text{sinc}(2\Delta\ell\omega_r\tau)] \right) \\ &\quad \times \exp \left[i \frac{\omega_r \tau}{2} \Delta\ell (2\bar{\ell} + \Delta\ell) \right]. \end{aligned} \quad (\text{S45})$$

In a similar fashion, one can evaluate the expectation value

$$\begin{aligned} \mathbb{E}(a_{\bar{\ell}+\Delta\ell} a_{\bar{\ell}+2\Delta\ell}^*) &\simeq \exp \left(-\frac{D\tau}{4\hbar^2} [1 - \text{sinc}(2\Delta\ell\omega_r\tau)] \right) \\ &\quad \times \exp \left[-i \frac{\omega_r \tau}{2} \Delta\ell (2\bar{\ell} + 3\Delta\ell) \right] \end{aligned} \quad (\text{S46})$$

It contains the same decoherence-induced decay as the expression above since only the relative angular momentum between the two superposition branches matters.

The expectation values containing $b_{\ell}^{\ell'}$ coefficients can be calculated by a straight-forward generalization replacing $v_{\ell}(t)$ by

$$v_{\ell}^{\ell'}(t) = \frac{er^2}{4}(\varepsilon_t e^{i2\ell'\omega_r\tau} e^{4i\ell\omega_r t} + \text{c.c.}). \quad (\text{S47})$$

This yields

$$\begin{aligned} \mathbb{E} \left[b_{\ell+\Delta\ell}^{\bar{\ell}+\Delta\ell} (b_{\ell+2\Delta\ell}^{\bar{\ell}})^* \right] &\simeq \exp \left(-\frac{D\tau}{4\hbar^2} [1 - \text{sinc}(2\Delta\ell\omega_r\tau)] \right) \\ &\times \exp \left[-i\frac{\omega_r\tau}{2} \Delta\ell(2\bar{\ell} + 3\Delta\ell) \right] \end{aligned} \quad (\text{S48})$$

and

$$\begin{aligned} \mathbb{E} \left[b_{\bar{\ell}+\Delta\ell}^{\bar{\ell}+\Delta\ell} (b_{\bar{\ell}+2\Delta\ell}^{\bar{\ell}})^* \right] &\simeq \exp \left(-\frac{D\tau}{4\hbar^2} [1 - \text{sinc}(2\Delta\ell\omega_r\tau)] \right) \\ &\times \exp \left[i\frac{\omega_r\tau}{2} \Delta\ell(2\bar{\ell} + \Delta\ell) \right]. \end{aligned} \quad (\text{S49})$$

Putting everything together, we obtain the measurement signal

$$P(D) = \frac{1}{2} - \frac{1}{2} \cos(\omega_r\tau\Delta\ell^2) C(\tau), \quad (\text{S50})$$

with the reduction factor of the Ramsey fringe contrast due to rotational decoherence

$$C(\tau) = \exp \left(-\frac{D\tau}{2\hbar^2} [1 - \text{sinc}(2\Delta\ell\omega_r\tau)] \right). \quad (\text{S51})$$